

The Standing Wave Phenomenon in Radio Telescopes

Frequency Modulation of the WSRT Primary Beam

A. Popping^{1,2} and R. Braun²

¹ Kapteyn Astronomical Institute, P.O. Box 800, 9700 AV Groningen, the Netherlands
e-mail: popping@astro.rug.nl

² Australia Telescope National Facility, CSIRO, P.O. Box 76, Epping, NSW 1710, Australia

ABSTRACT

Context. Inadequacies in the knowledge of the primary beam response of current interferometric arrays often form a limitation to the image fidelity, particularly when “mosaicing” over multiple telescope pointings.

Aims. We hope to overcome these limitations by constructing a frequency-resolved, full-polarization empirical model for the primary beam of the Westerbork Synthesis Radio Telescope (WSRT).

Methods. Holographic observations, sampling angular scales between about 5 arcmin and 11 degrees, were obtained of a bright compact source (3C147). These permitted measurement of voltage response patterns for seven of the fourteen telescopes in the array and allowed calculation of the mean cross-correlated power beam. Good sampling of the main-lobe, near-in, and far-side-lobes out to a radius of more than 5 degrees was obtained.

Results. A robust empirical beam model was determined in all polarization products (XX , XY , YX and YY) and at frequencies between 1322 and 1457 MHz with 1 MHz resolution. Substantial departures from axi-symmetry are apparent in the main-lobe as well as systematic differences between the polarization properties. Surprisingly, many beam properties are modulated at the 5 to 10% level with changing frequency. These include: (1) the main beam area, (2) the side-lobe to main-lobe power ratio, and (3) the effective telescope aperture. These semi-sinusoidal modulations have a basic period of about 17 MHz, consistent with the natural “standing wave” period of a 8.75 m focal distance. The deduced frequency modulations of the beam pattern were verified in an independent long duration observation using compact continuum sources at very large off-axis distances.

Conclusions. Application of our frequency-resolved beam model should enable higher dynamic range and improved image fidelity for interferometric observations in complex fields, although at the expense of an increased computational load. The beam modulation with frequency can not be as easily overcome in total power observations. In that case it may prove effective to combat the underlying multi-path interference by coating all shadowed telescope surfaces with a broad-band isotropic scattering treatment.

Key words. Polarization – Scattering – Techniques: image processing – Techniques: interferometric – Techniques: spectroscopic – Telescopes

1. Introduction

For any telescope it is essential to know the shape of the point spread function as well as the effective field-of-view, since we can only see the true sky as filtered by these response patterns. In the case of an earth-rotation-synthesis interferometric array, the effective field-of-view is determined by the complex product of each pair of voltage response patterns of the telescopes in that array. However, for most synthesis arrays, the precise shape of this so-called “primary beam” is not known. For example the primary beam of the 25 m prime-focus-fed parabolic dishes of the Westerbork Synthesis Radio Telescope (WSRT) is approximated by the $\cos^6(cvr)$ analytic function. In this function, r is the distance from the pointing center in degrees, v the

observing frequency in GHz and the constant $c = 68$ is, to first order, wavelength independent at GHz frequencies.

This approximation assumes an axi-symmetric beam shape which consists of just the main lobe and does not include any side-lobes. For real radio telescopes however, like the WSRT, the sensitivity is not confined to the main beam, but spread out over the full 4π rad². The telescopes are primarily sensitive in the main beam, but a significant contribution comes from outside the main beam. Response from outside the main beam is referred to as *side lobes* or *stray radiation* (Hartmann et al. 1996). These features can be caused by parts of the aperture which are blocked by the feed and support structures (Napier 1999) as well as by irregularities of the reflector surface. Radiation may be received directly into the feed, but also after scattering off the feed support legs.

van Woerden (1962) was the first observer to interpret temporal variations in H I spectra as due to side lobes or stray radiation. Kalberla et al. (1980) documented stray radiation problems for the Effelsberg telescope. Similar investigations have been made for the Dwingeloo 25 meter telescope by van Woerden (1962), by van Woerden et al. (1962), and by Raimond (1966). From these investigations it is obvious that essentially all observations made with parabolic radio antennae are affected by stray radiation at some level.

Another phenomenon plaguing spectroscopic observations in radio astronomy is the so-called “standing wave” phenomenon (Briggs et al. 1997). The term “standing waves” is used to describe a semi-periodic variation in the spectral band-pass seen in many radio telescopes which has a basic wavelength of approximately $c/(2f)$ Hz, for focal distance, f , (or about 17 MHz for the WSRT dishes). As we will show below, this phenomenon is closely tied to variations in the primary beam properties with frequency.

The antenna pattern of the 25 m telescope in Dwingeloo has been studied in detail by Higgs (1967). So-called “stray cones” are associated with radiation scattered from the feed support legs, while a “spillover ring” is associated with radiation reaching the feed from just beyond the edge of the reflector. Kalberla et al. (1980) measured the antenna pattern of the 100 m Effelsberg telescope to a radius of 2 degrees from the main beam axis and created an empirical model of the far side lobes. Observations were done several times at different hour angles and at various epochs, which provided the material necessary to determine the relative amplitudes of the various components of the model. The empirical model Kalberla developed contained a spillover ring, four stray cones (from radiation scattered off the feed support legs), and a blockage (or “shadowing”) contribution due to the support legs. Reflections from the roof of the apex cabin resulted in four small additional components. With this work, Kalberla demonstrated that the main beam and side lobes could be effectively modelled, using careful measurements of the sky brightness distribution.

The WSRT is comparable to many other radio telescopes in the sense that it has feed- and feed-support structure blockages, which influence the shape of the beam. Departures from axi-symmetry and side-lobes are present, but are neglected in the current beam approximation. The approximation is truncated above the level of the first side lobes, which directly limits the fidelity of a primary-beam-corrected image. Image fidelity could be substantially improved with a better model. A related problem arises when one is combining data obtained at a series of different pointing centers, in a process termed mosaicing (Cornwell 1989), since an accurate model of the primary beam is required when undertaking a joint deconvolution of all data. The dynamic range in the resulting combined image is determined (amongst other things) by the quality of the primary beam model.

Although a simple approximation is used for most radio telescopes, a specific detailed model would need to be developed for each individually. We are particularly interested in utilizing an improved beam model for the WSRT and will develop that model here. The WSRT is an aperture synthesis interferometer that consists of a linear array of 14 antennas ar-

ranged on a 2.7 km East-West line. Ten of the telescopes are on fixed mountings while the remaining four dishes are movable along two rail-tracks. The antennas are equatorially mounted 25-m dishes (with an f/D ratio of 0.35) and are fed from the prime focus. A major advantage of the equatorial mounting is that the primary beam does not rotate on the sky while tracking (Napier 1999) as it does for the elevation-over-azimuth mount (Thompson et al. 1986).

The WSRT array is equipped with Multi Frequency Front Ends (MFFE), which have cooled receivers at 3.6, 6, 13, 18+21 cm, and uncooled receivers at 49 cm and 92 cm. The 21 cm receiver is used most extensively and in this paper we will only consider beam properties in this wavelength band. We develop a detailed numerical representation of the WSRT-primary beam; not just including the main lobe, but also the side lobes. Furthermore, we consider all four polarization products individually rather than just Stokes I. And most importantly we consider the variation of beam properties with frequency at a resolution sufficiently fine (1 MHz) to fully sample the so-called “standing wave” phenomenon. The paper is organized as follows. In section 2 we briefly describe the relationship between aperture illumination and the beam pattern of a telescope. Section 3 describes the method used to determine our model and in section 4 the results are presented. The model is tested with observations of celestial sources in section 5. In the summary and discussion of section 6 we consider how frequency modulation of beam parameters can be dealt with, both for interferometric and total power observations.

2. Theory

We will briefly consider the relationship between aperture illumination and a radio telescope beam. This will be useful when we describe how we arrive at our beam representation in the next section. The relation between the complex aperture pattern of the antenna, $f(u, v)$, and the complex voltage-beam pattern, $F(l, m)$, of the antenna (Kraus 1986) is:

$$F(l, m) = \iint_{\text{aperture}} f(u, v) e^{2\pi i(ul+vm)} du dv \quad (1)$$

and

$$f(u, v) = \int_{-\infty}^{\infty} \int_{-\infty}^{\infty} F(l, m) e^{-2\pi i(ul+vm)} dl dm \quad (2)$$

The coordinates of the radiation pattern are given by

$$u = \sin \theta \cos \phi \quad \text{and} \quad v = \sin \theta \sin \phi \quad (3)$$

This Fourier transform relationship between antenna and voltage-beam pattern is analogous to the one between the source brightness distribution and the visibility function that is sampled by an interferometer. The aperture distribution $f(u, v)$, is determined by the way in which the antenna feed illuminates the aperture together with how the aperture is blocked, as is described in detail by Napier (1999). In general, the more that $f(u, v)$ is tapered at the edge of the aperture, the lower will be the aperture efficiency and the side lobes and the broader the

main beam. The Fourier transform of the aperture can be described in terms of *amplitude* and *phase* or the real and imaginary parts, $(a+ib)$. In the case of a single dish telescope or when calculating auto-correlations, the power patterns are given by $F \cdot F^*$, which gives

$$(a + ib) \times (a - ib) = a^2 + b^2 \quad (4)$$

In the case of cross-correlations, when using different telescopes, the power pattern is given by $(F \cdot G^* + G \cdot F^*)/2$, which gives

$$\frac{(a + ib) \times (c - id) + (c + ib) \times (a - ib)}{2} = ac + bd \quad (5)$$

3. Method

An analytic model would be the most convenient way to describe the beam pattern. This could be used to predict the beam parameters at any desired position without the need for interpolation and would be easy to implement in software. However as we will show below, an analytic model is not sufficient to describe the actual telescope beams and an empirical model is required. A straightforward way to get the actual beam shape of a telescope is by measuring its voltage pattern with a holographic measurement (Scott & Ryle (1977); Kraus (1986)). A pair of antennas is needed; whereby one of the antennas continuously tracks a strong point source and the other antenna scans the vicinity of that source. The voltage pattern $F(l, m)$ is obtained from the complex correlation coefficient of the scanning antenna with respect to the reference antenna. Once the voltage pattern is known the auto-correlation power beam can be obtained by multiplying with the complex conjugate. Alternatively, the interferometric cross-correlation power beam can be obtained by multiplying voltage patterns and their complex conjugates in a pair-wise fashion and averaging the result. Our model is based on this concept of holographic measurements, although it is extended by combining a series of measurements that sample a wide range of angular scales.

3.1. Holographic Measurements

Three holographic observations were carried out, with different fields of view to obtain sampling at high, medium and low resolution. The smallest field of view sampled 2.2×2.2 degrees with 25×25 samples, the medium, 7.26×7.26 degrees with 33×33 samples and the large, 11×11 degrees with 25×25 samples. For each observation 8 bands of 20 MHz bandwidth were observed with 8×64 spectral channels and the 4 linear polarization products: XX , XY , YX and YY . Of the 20 MHz of each band, about 18 MHz are useful due to the roll-off of the intermediate frequency filters at the edge of the band. The bands were centered at 1450, 1432, 1410, 1392, 1370, 1350, 1330, 1311 MHz. The frequencies were selected to avoid Galactic neutral hydrogen emission and known radio frequency interference (RFI eg. near 1380 MHz).

Of the 14 telescopes in the array, the seven even-numbered telescopes were used as reference antennas and the seven odd-numbered were used for scanning the vicinity of 3C147. A 10

second basic integration time was employed, with 30 seconds nominal dwell time on each position in the scanning pattern. Data acquired during telescope movement was flagged, yielding 20 seconds of net integration time per position. The voltage beams were obtained from the holographic measurements using the MSHOLOG code developed by H. van Someren Greve. This code calibrates out constant phase offsets between antennas and compensates for the small geometrical delays that arise when scanning telescopes are pointed off-axis. An optional Wiener filtering can be employed within MSHOLOG to limit the occurrence of signal in the aperture plane to only the surface of the reflector, while interpolating in the far-field sampling pattern. We have not employed this option, but chose only to grid the calibrated data. Each voltage beam has a real and imaginary part, which can be recast as amplitude and phase. An important choice in the processing is the number of spectral channels to bin together. Binning more channels improves the signal-to-noise ratio, but degrades the spectral resolution. We chose to bin each group of two consecutive channels, yielding 0.625 MHz spectral resolution. Individual voltage beam images were inspected and an occasional grid-point was replaced with a linearly interpolated value when large deviations were apparent. In the handful of cases where excessive deviations were encountered in the entire pattern, i.e. when the data quality was not sufficient, that specific pattern was not included in the subsequent processing.

The pair-wise (complex conjugate) products of the seven available voltage beams yielded 21 distinct baseline power beams. These were averaged to yield the mean interferometric power beam. All power beams were normalised to a peak height of unity. The average dispersion of a single combination of antennas with respect to the mean power beam is 0.2%. This number is determined by calculating the dispersion of each combination at each frequency and taking the mean value of these individual dispersions. For this purpose we only made use of the holographic measurements with a small field of view, mapping the main beam at high resolution.

3.2. Combining Measurements

The mean power beams at three different scales need to be combined to get the most complete representation of the beam. The small field provides detailed information about the center of the beam, the medium field samples intermediate scales, while the large field samples the outer side lobes.

To combine the images, the sampling of the three measurements should ideally be the same. This can be accomplished with a *Sinc* function interpolation by Fourier transforming the medium and large field data to the aperture plane and padding out in the transform plane with zeros before Fourier transforming back to the image plane. The sampling of our small field was chosen to be exactly five times as fine as our large field and 2.5 times as fine as the medium field. So padding the Fourier transform of our medium field out to 2.5 times the size and our large field to five times the image size before Fourier transforming back yields identical image plane sampling for all three power beams. The difference is only the spatial ex-

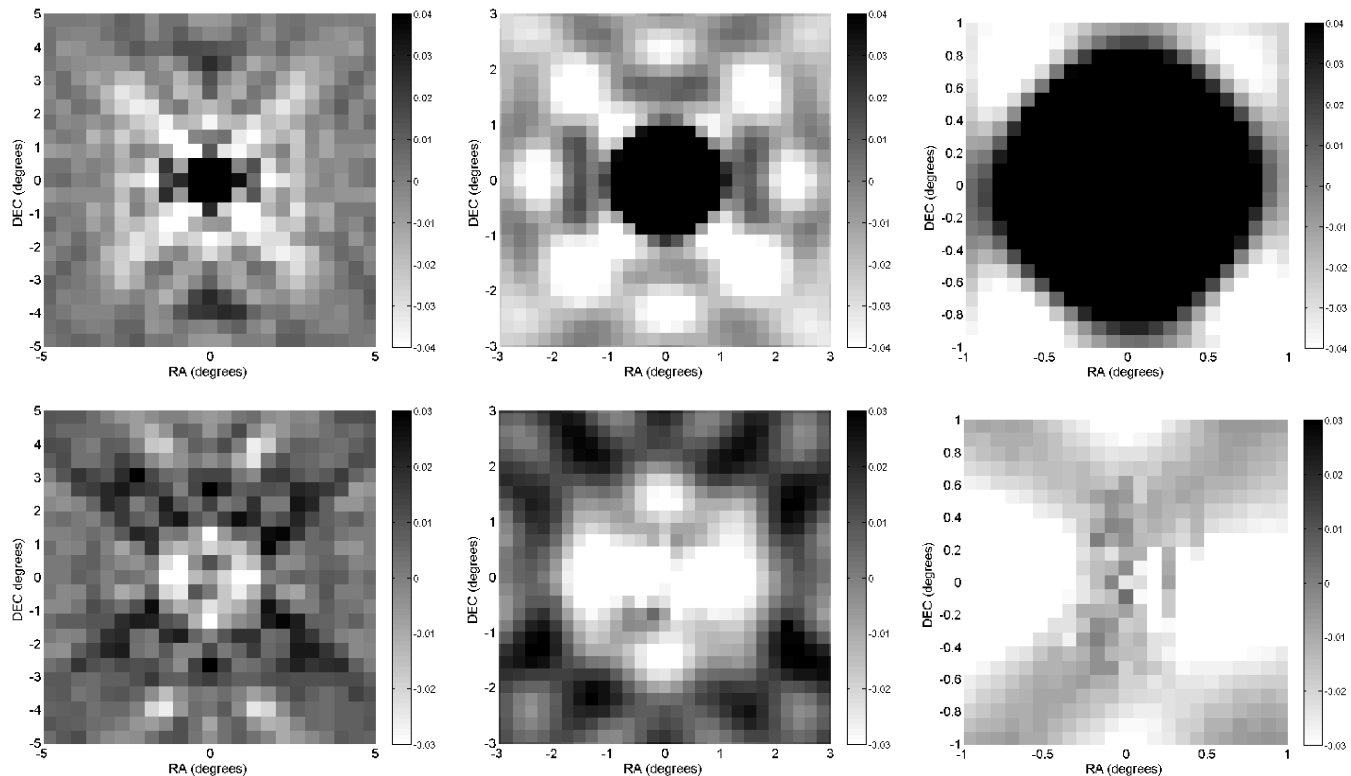


Fig. 1. PSFs of the voltage pattern of polarisation X at 1416.6 MHz for the three different holographic measurement scales, averaged over all the antennas. From left to right is the large, medium and small field of view. The top panels show the *cosine* (real) values and the bottom panels show the corresponding *sine* (imaginary) values. All images are on a linear scale, although for the real images only a small range is plotted at the level of the sidelobes. The peak values of the voltage patterns are normalised to unity.

tent provided by each, which has not changed. Beginning with the resampled large beam, the inner 7.26×7.26 degrees were first replaced with the resampled medium beam and finally the inner 2.2×2.2 degrees were replaced with the measured small beam. Minor discontinuities between the different coverages were smoothed out by taking the average within a 0.25 degree wide border zone around the medium and small beams rather than taking the simple replacement as done inside this zone.

It is quite instructive to consider both the image and aperture plane features that are apparent on the three observed scales. An example of the three observed voltage beam scales is shown in Fig. 1, while the corresponding aperture distributions are shown in Fig. 2. The large field image has an aperture distribution which is only slightly larger than the size of the telescope surface. The resolution is moderately high, yielding a detailed view of the shadowed parts of the telescope surface. The feed-support legs can be clearly seen as well as the triangular shadows that these legs cast on the outer reflector surface. The top right support leg has a slightly larger electrical cross-section than the other three since the cables from the receiver package also run along it. Remarkably, there is significant signal intensity from the blocked parts of the aperture; for example under the receiver. Geometric optics would preclude signal intensity from such regions. Interestingly, large phase offsets are seen at these locations, especially at the apex and around the feed-support legs. The radiation reaching the receiver from

these locations is apparently *anti-correlated*, actively diminishing detected signal strength rather than merely adding incoherent noise.

3.3. Beam Model Cubes

Beam models were produced for every pair of observed frequency channels (yielding 0.625 MHz resolution). The first and last few channels of each observed 20 MHz band were not used, because of the roll-off of the bandpass. Given the 8 band centers noted previously, almost complete frequency coverage between 1322 and 1457 MHz was available. An interpolation was done between the separate models to determine a model at each integer MHz within this range. Since voltage beams were available in the X and the Y polarization, power beams could be calculated for all four polarization products: XX , YY , XY and YX .

4. Results

By using holographic measurements at different sampling scales, we can construct an empirical model, that describes the primary beam of the WSRT with high precision at different frequencies. A Point Spread Function of the Stokes I polarisation is shown in Fig. 3 where the beam is averaged over a bandwidth of about 16 MHz. The main beam has a clear “diamond” shape and around the main beam there is a sharp dip, corre-

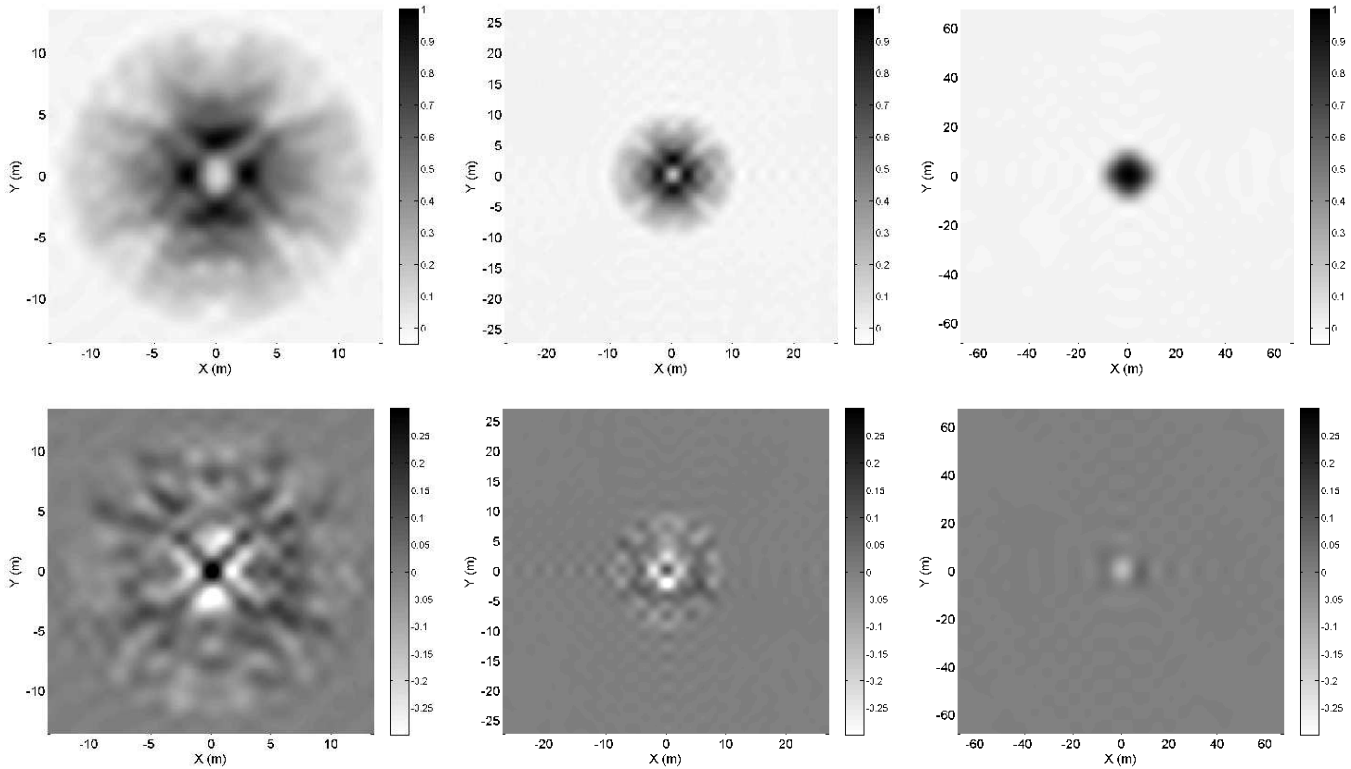


Fig. 2. Aperture patterns corresponding to the voltage patterns in Fig. 1. The large field of view gives the most detailed description of the antenna, showing clearly the regions blocked by the receiver and support structure. Phase deviations are largest within the blocked regions of the aperture.

sponding to the first null. Note that this first null can only be discerned when holographic measurements are sampled at very high resolution in the image plane (and not the aperture plane as is usual) together with suitably high frequency resolution. The outer sidelobes show a clear “cross” pattern, due to blockage of the support structure.

Many significant variations can be seen in the model beams as function of frequency. Channel maps of the Stokes I -model are shown in Fig. 4, starting at 1442 MHz, and going down to 1427 MHz with intervals of 3 MHz. Because of the small scale in this plot, possible variations in beam-width are difficult to discern visually. However, there is an easily discernible variation in the strength of side-lobe structures. For example, at 1433 MHz the first side lobes are very weak compared to 1430 MHz. On the other hand, the more distant side lobes almost vanish at 1430 MHz. No extended sidelobes are seen at 1430 MHz, while at 1439 and 1436 MHz a very clear diffuse “cross” is apparent. The panels in the figure span 15 MHz of bandwidth which is almost one full period in the periodic variations. These variations are representative of those seen throughout the full frequency coverage of our model. There are several ways to visualise the frequency dependence of the beam and of the side lobes with respect to the main beam. Variations in the main beam properties can be illustrated by evaluating the beam integral at all frequencies. This was accomplished with an elliptical Gaussian fit to each beam using the IMFIT task of the MIRIAD package (Sault et al. 1995). The values are plotted against frequency in Fig. 5 for both the XX and YY polarisations

after smoothing over 3 MHz. Very similar patterns are seen in both cases, although the beam areas for the XX polarisation are systematically larger by about 2%. Similar results are obtained by simply taking the sum of the relevant image pixels within the main lobe, although the discrete sampling introduces additional quantization noise.

As expected, the beam area decreases approximately quadratically with increasing frequency, since the beamwidth should vary roughly as λ/D . More remarkable are the semi-periodic oscillations. Both polarizations display a similar periodicity of ~ 17 MHz with an amplitude of about $\sim 4\%$ in surface area.

An estimate of the side-lobe power can be obtained from the difference of the integral over $11 \times 11^\circ$ with the main-lobe integral based on the elliptical Gaussian fit as described above. The integrated main-lobe and side-lobe powers as a function of frequency are shown for Stokes I after normalisation to a mean value of unity in Fig. 6 (dotted and dash-dotted line) together with the ratio between side-lobe and main-lobe power (solid line). This ratio gives the fraction of the power that is contained in the sidelobes, independent of any scaling. The same periodicities can be seen as in the previous plot, for both the main beam and the side lobes, although the variations in the integrated side lobe power are stronger and are of the order of $\sim 20\%$.

An important aspect of the comparison of beam attributes with frequency is the normalisation that has been applied. Since the peak image-plane response of each model beam has been

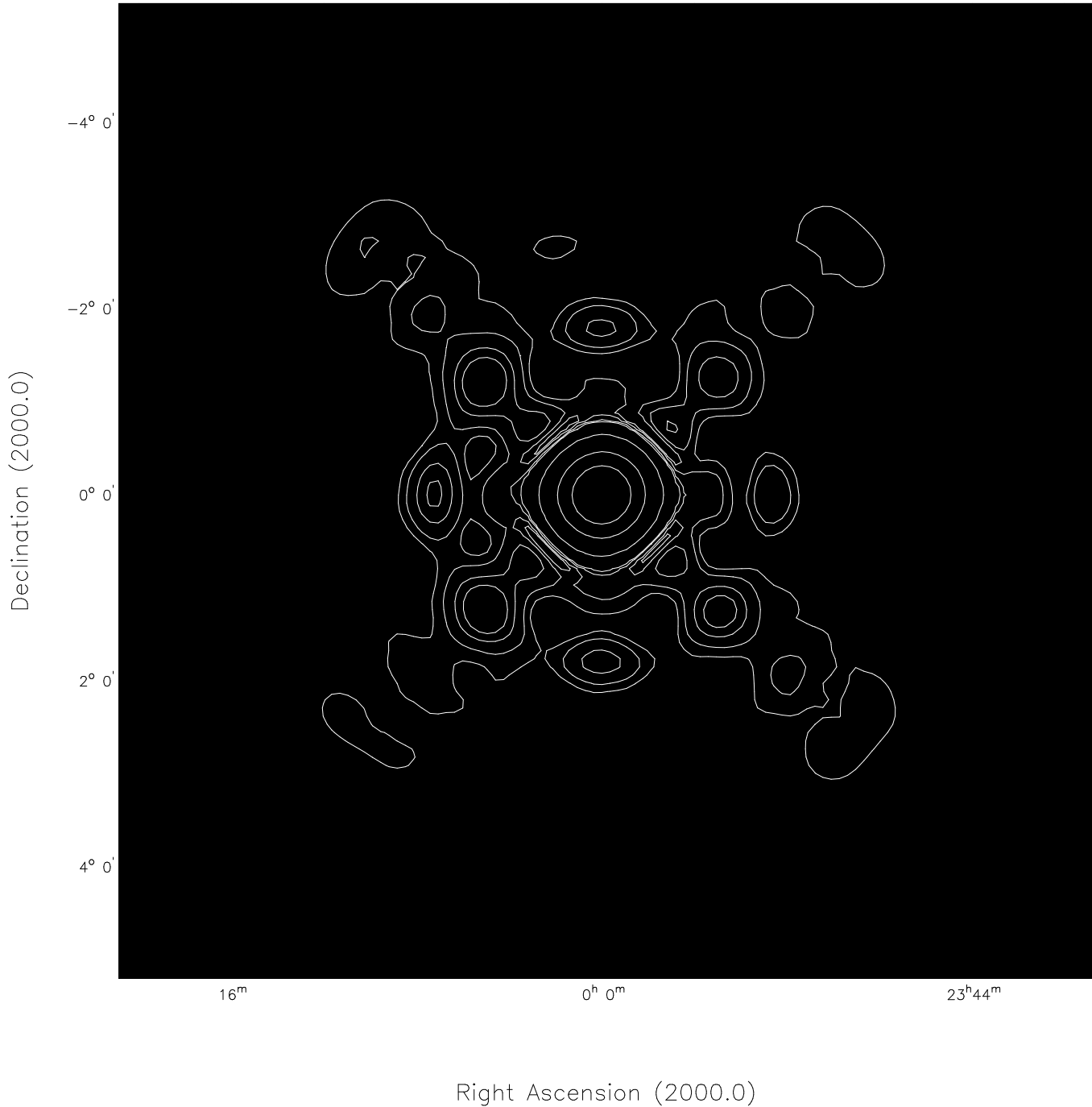


Fig. 3. PSF of the beam model averaged over 16.25 MHz (50 channels) around 1391.7 MHz. The average of the XX and YY polarisations is plotted, corresponding to Stokes I , such as commonly used for correcting the primary beam in reduction software. Contour levels are drawn at 0.0005, 0.001, 0.002 0.003, 0.03 0.2 and 0.5, the peak value is normalised to 1.

set to unity, no information is preserved regarding the absolute telescope gain as a function of frequency. This is important, since normally one might assume that a smaller main beam area might correspond to a higher telescope gain, for example via a more uniform aperture illumination pattern. Such straightforward associations may not necessarily apply.

A convenient method of determining the telescope gain as function of frequency is available for an interferometer if both

auto- and cross- correlation spectra are measured. This is done by taking the cross-correlation spectrum of a pair of telescopes, $\rho_{12}(\nu)$, when observing a bright calibration source and dividing it by the square root of the product of the two auto-correlation spectra of these same telescopes, $\rho_{11}(\nu)$ and $\rho_{22}(\nu)$. In terms

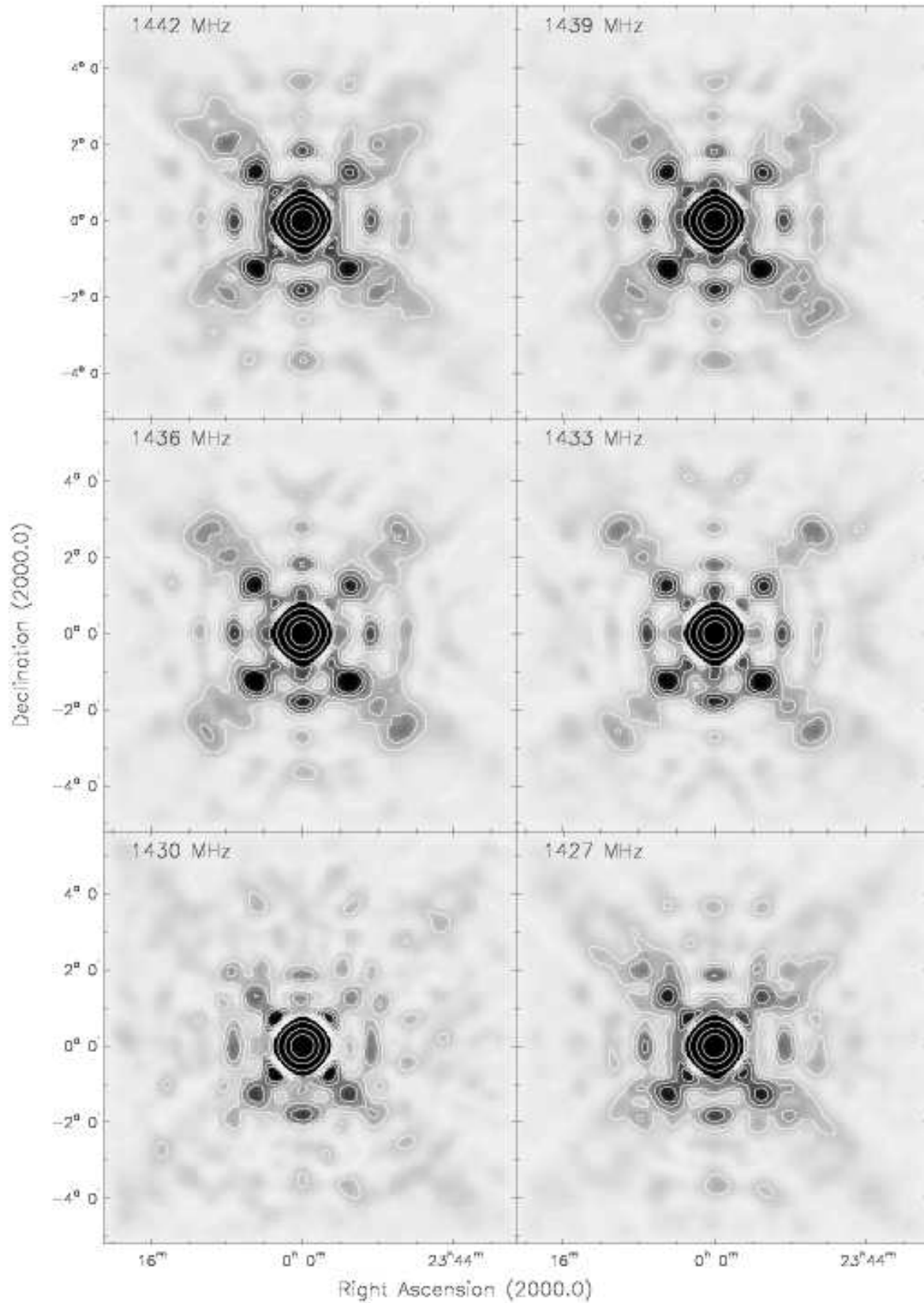


Fig. 4. Channel maps of the model cube for Stokes I between 1442 and 1427 MHz. Clear variations can be seen in the first and second side lobe structures. Contour levels are drawn at 0.0005, 0.001, 0.002, 0.003, 0.03, 0.2 and 0.5.

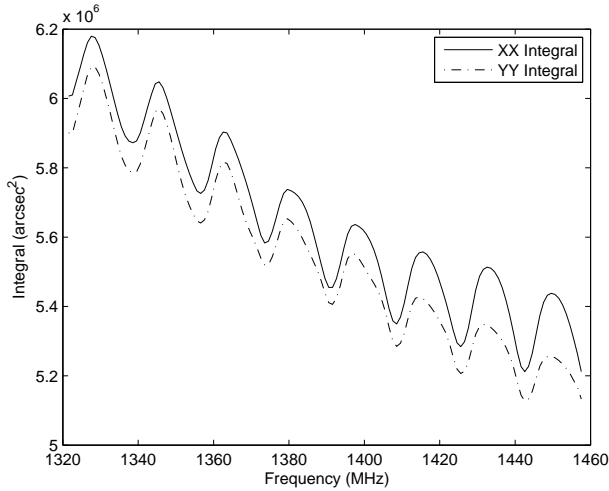


Fig. 5. Main beam integral, evaluated from a 2D Gaussian fit for the XX and YY polarizations as function of frequency. For increasing frequency the beam integral is decreasing quadratically as expected. However, there is a systematic variation with a ~ 17 MHz period.

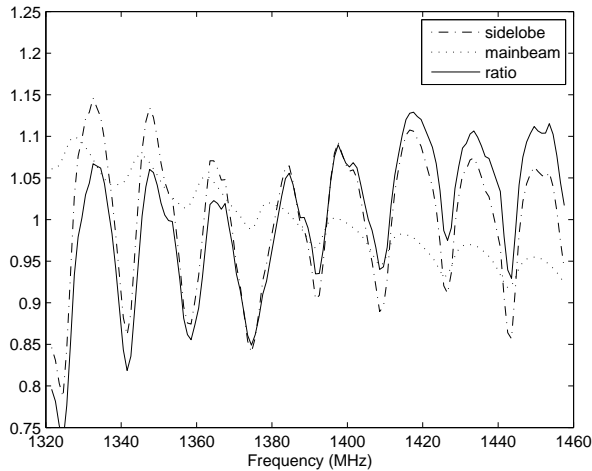


Fig. 6. Integrated side-lobe power (dash dotted line), integrated main beam power (dotted line) and the side-lobe to main beam power ratio (solid line) for Stokes I . All three lines are scaled to a mean value of one.

of the effective aperture A , the source flux density, S , and the bandpass shape, F , one gets,

$$\rho_{12}(\nu) \propto \frac{A(\nu) \cdot S(\nu) \cdot F_1(\nu) \cdot F_2(\nu)}{[T_{sys} + T_{sou}(\nu)]} \quad (6)$$

and

$$\rho_{11}(\nu) \propto [T_{sys} + T_{sou}(\nu)] \cdot F_1(\nu) \cdot F_1(\nu) \quad (7)$$

so

$$\frac{\rho_{12}(\nu)}{\sqrt{\rho_{11}(\nu) \cdot \rho_{22}(\nu)}} \propto \frac{A(\nu) \cdot S(\nu)}{[T_{sys} + T_{sou}(\nu)]^2} \quad (8)$$

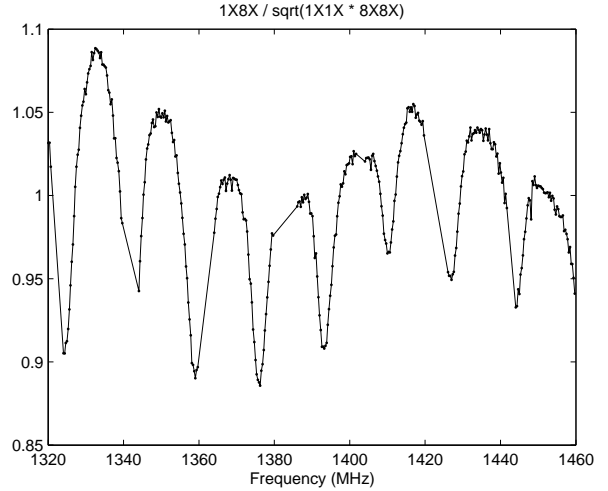


Fig. 7. cross-correlations of antenna 1 and 8 divided by the auto-correlation of these two antennas. The variation has a period of ~ 17 MHz.

where the system temperature is made up of a source independent component, T_{sys} and the contribution due to the observed source, $T_{sou}(\nu)$. The bandpass shape of both receiver chains cancels out in this combination, and one is left with the gain spectrum of the interferometer (together with possible frequency structure of the calibration source). The receiver temperature due to the observed source will in turn be proportional to $A(\nu)$, so if this were neglected it would lead to a dilution of any possible variation of effective aperture with frequency. In practise, 3C147 increases the system temperature by only 8% for the WSRT system near 1400 MHz, so this dilution effect could be compensated by simply multiplying the deduced gain variations by a factor of 1.002. The derived gain is plotted for two representative telescopes (RT1 and RT8) in the X polarization in Fig. 7 using one of our holographic observations of 3C147 during an interval when both the reference and scanning telescopes are pointed at the source. Very substantial oscillations of 5 to 10% amplitude are seen with a similar period of ~ 17 MHz. Comparing the system gain with the main and side-lobe powers in Fig. 8 illustrates the counter-intuitive result that the highest gain is accompanied by both the largest beam area and the highest ratios of side- to main-lobe power.

One way in which to partially understand these correspondences is to consider that the broadest main-beam patterns may correspond to the instances of highest effective illumination of the central portions of the aperture with respect to the outer portions of the aperture. This might occur when a minimum amount of radiation (with inappropriate phase) reaches the feed after reflection from the central blockage (in the shadow of the receiver package). At other portions of the cycle, a larger amount of radiation from this region would reach the feed, causing both a decrease in gain (in view of the detrimental phase) as well as a narrower main beam, since the central portion of the reflector would contribute negatively. What remains difficult to explain, is why the side-lobe levels would be lowest when the gain was lowest.

Source	Right Ascension (hms)	Declination (dms)	Radius (arcsec)	\cos^6 flux (Jy)	model flux (Jy)	NVSS flux (Jy)
A	8:21:29	+70:14:33	1904	115.3	107.7	101.8
B	8:22:16	+70:53:08	1124	613.5	605.4	602.3
C	8:21:33	+71:07:43	1658	125.3	125.4	116.3
D	8:21:31	+71:19:41	2309	975.0	1012.5	961.9

Table 1. Data for some extreme off-axis sources found in the Holmberg II field. The distance from the primary beam center is given in the fourth column. The fifth and sixth column give the average flux of all the narrow band images (for an effective frequency of 1360 MHz) after primary beam correction with both the \cos^6 beam description and the new empirical model. The NVSS flux at 1400 MHz is given in the last column.

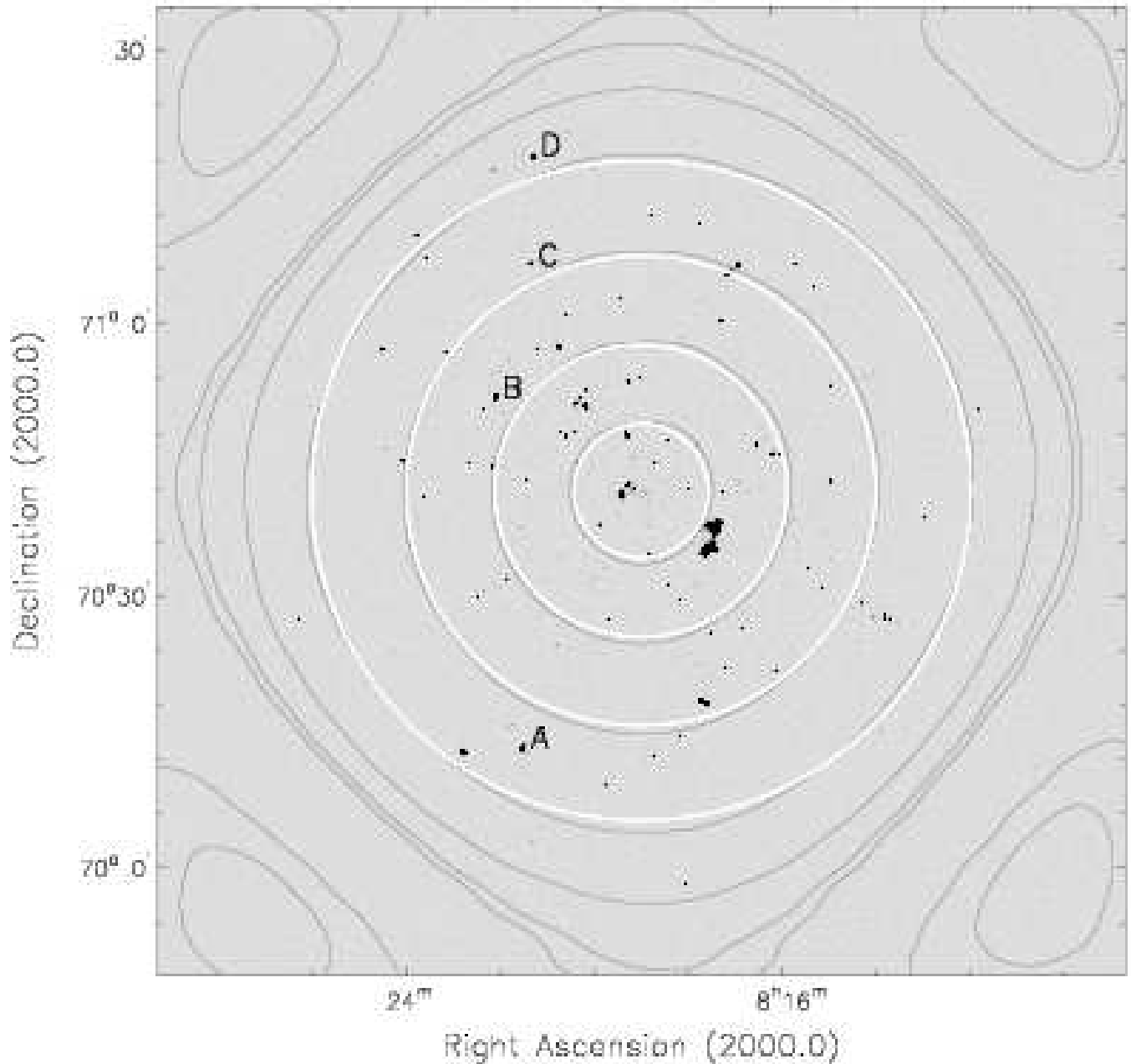


Fig. 9. WSRT image of the Ho II field. The white contours represent the old \cos^6 beam description, the contour levels from inside out are at 0.9, 0.5, 0.2 and 0.05. The gray contours correspond to the new model, the levels are at 0.9, 0.5, 0.2, 0.05, 0.01, 0.003 and 0.002. In the corners of the field, the first sidelobes can be clearly recognized. Letters are assigned to those sources for which we show the beam-corrected flux as function of frequency in Fig. 10.

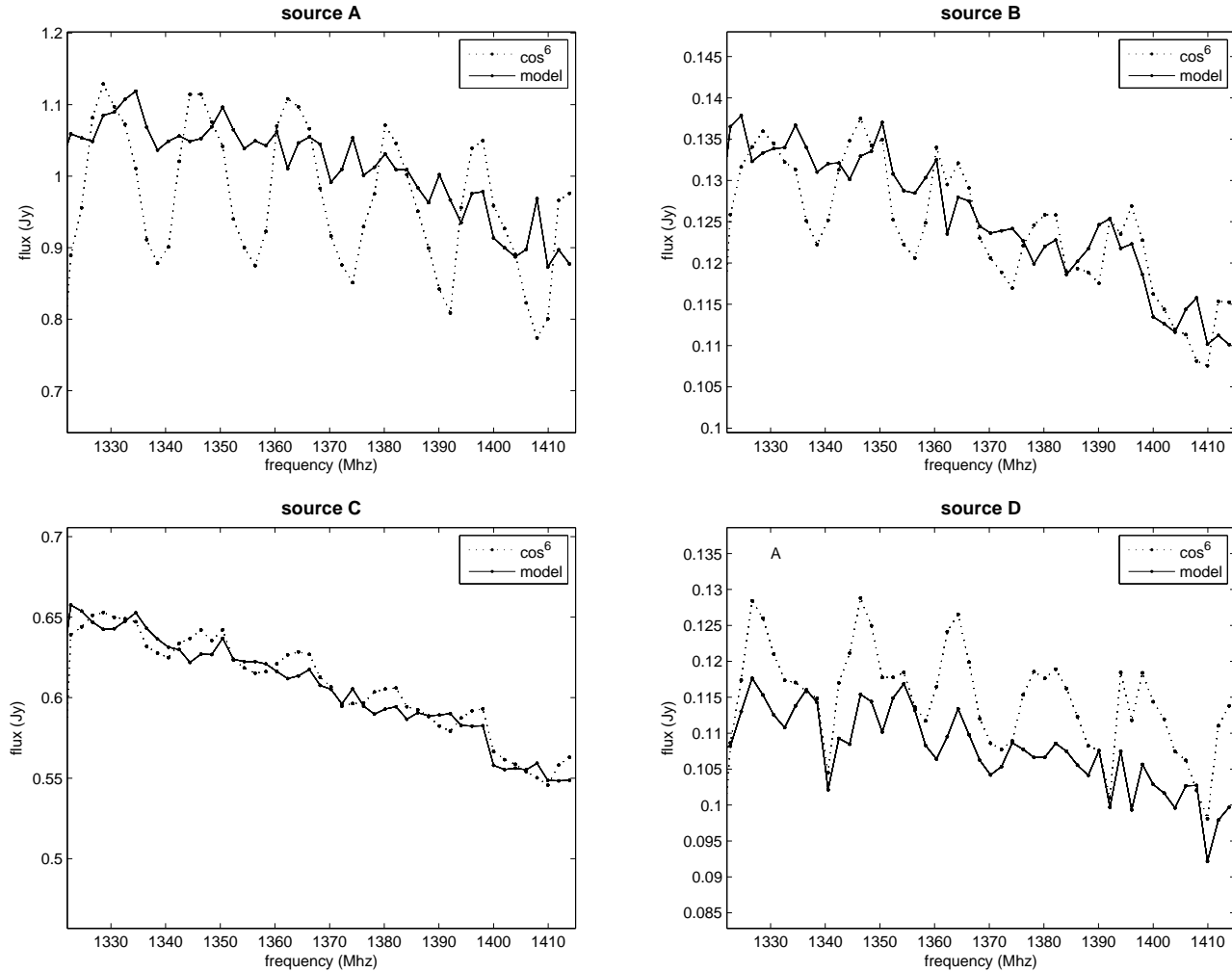


Fig. 10. Fluxes are plotted as function of frequency for sources in Table 1 after primary beam correction. The solid lines correspond to a correction with our empirical model, while the dotted lines are corrected using the \cos^6 beam approximation.

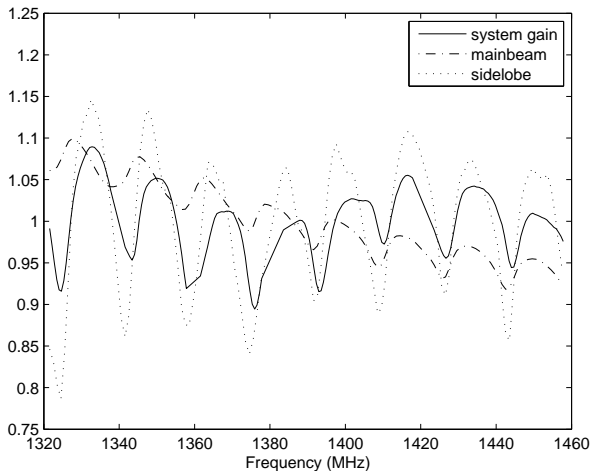


Fig. 8. The smoothed gain ripple (solid line), and integrated values for the main beam (dash dotted line)

5. Testing with Celestial Sources

Although we have confidence in our methodology, it is important to verify the rather remarkable variations in beam parameters with frequency which we derive, using independent observations under typical observing conditions.

A suitable source of single field observations is the recently published WSRT SINGS survey Braun et al. (2007). We have produced calibrated, deconvolved images from this survey database for four different fields centered on the nearby galaxies Holmberg II, IC 2574, NGC 2841 and NGC 5194 at frequencies between 1322 and 1408 MHz at increments of 2 MHz. Unresolved and unconfused sources were sought in each of these fields with a high enough apparent brightness that they could be detected with good signal-to-noise in the narrow bandwidth images. The most interesting sources are those that are bright, but very far from the pointing center since they probe the largest primary beam corrections. We overlay the \cos^6 and our empirical primary beam attenuation model on the field of Ho II in Fig. 9 to illustrate how the apparent density of sources varies with position. Comparison of contours from the two types of beam model suggests that small depar-

tures from axi-symmetry already set in at relatively high levels. The best test sources found in the four different fields are listed in Table 1. We also tabulate the NVSS (NRAO VLA Sky Survey, Condon et al. (1998)) 1.4 GHz flux densities of these sources together with the averaged (ie. 1360 MHz) flux density obtained from both the \cos^6 function and our empirical model. Reasonable agreement can be found between the flux values, although the fluxes we measure at 1360 MHz are systematically higher than seen in the NVSS (at effective frequency of 1400 MHz) likely due to the negative mean spectral index of background sources.

We plot the primary beam corrected flux densities of several test sources in Fig. 10. In the figures we contrast the flux densities obtained by applying the $\cos^6(cvr)$ model and our empirical primary beam attenuation model. The improvement in recovering a plausible, smoothly varying spectrum (and of course the correct mean flux density) for the off-axis sources is striking. In the case of source A, there is a very strong variation in the flux with frequency. When using the new model, the 17 MHz variation is flattened out and only smaller noisy fluctuations remain. A quite similar effect is apparent in source B and source D. Of course the new model does not predict substantial differences from the historical analytic model at all positions within the beam. An example is given with source C, where mean flux levels are comparable, although the low level periodic variation is eliminated with the new model.

6. Summary and Discussion

In this paper we develop a frequency-resolved empirical model of the primary beam of the WSRT 25m antennas between 1320 and 1460 MHz in two orthogonal linear polarizations. This is based on a series of holographic measurements sampling a wide range of angular scales from about five arcmin to 11 degrees. Not surprisingly, there are significant departures from axi-symmetry in the form of a “diamond” distortion of the main lobe due to the quadrapod blockage of the telescope aperture. This aperture blockage also gives rise to a four-fold symmetry in the side-lobe pattern within a radius of about five degrees. Systematic differences are also apparent in the two perpendicular polarizations, in the sense that beam areas are about 2% larger in the *XX* polarization than the *YY*. Furthermore the beam shapes are not symmetric, but there is a slight ellipticity; elongated in the direction of the polarization. For the *XX* polarization, the beam is about 4% larger in the *x*-direction, compared to the perpendicular *y*-direction. For the *YY* polarization we see an elongation in the *y*-direction, although here the difference is only about 2.5% relative to *x*.

More surprisingly, we document systematic oscillations in the beam properties as a function of frequency. A similar semi-sinusoidal variation is found for each of: (1) the integrated beam area, (2) the ratio of integrated side-lobe to main-lobe power and (3) the effective aperture of the telescope system. All three of these attributes are modulated at the 5 to 10% level with a basic periodicity of about 17 MHz, corresponding to the natural “standing wave” period of about $c/2f$ for a paraboloid of focal distance, $f = 8.75$ m. These effects are manifestations

of constructive and destructive interference occurring at the telescope feed caused by multi-path transmission.

We have verified these deduced oscillations in beam properties with independent measurements under typical observing conditions; namely long duration tracks employing earth rotation synthesis. A crucial aspect here is that the WSRT telescopes employ an equatorial mount, so that the beam patterns are at least fixed on the sky despite tracking a field for many hours. Although the on-axis frequency response has been effectively calibrated in such observations, continuum sources which are sufficiently far off-axis display a modulation in their apparent flux density with frequency. Application of our empirical beam model effectively removes such off-axis modulation of apparent flux density with frequency. While this procedure permits effective correction of interferometric observations (employing an equatorial mount), albeit at a substantially increased complexity of processing, there is no comparable correction procedure for total power measurements which suffer from the same effect. Improving the spectral baselines of total power observations will require a method of physically eliminating such modulations from the telescope/feed system.

The primary surfaces which contribute to these interference effects are those portions of the main reflector which suffer from geometrical blockage; the regions “under” the feed-support legs and prime focus receiver support structure (as seen from the sky) together with those parts of the reflector which are “behind” the feed-support legs as seen from the feed. And finally, the surfaces of the feed-support legs themselves which are directly visible from the feed. Since coherent reflections from these surfaces appear to be responsible for the oscillations in antenna beam properties with frequency we suggest that a likely remedy for these effects would be a surface treatment of all of the aforementioned surfaces to make them behave as broad-band isotropic scatterers rather than coherent reflectors. Scattering is preferred over absorption since large absorbing surfaces at ambient temperature on the reflector and telescope structure will adversely affect the system temperature.

Design of a broad-band isotropic reflector could be achieved by taking a white noise distribution, applying a suitable power-law of radius taper and Fourier transforming this distribution. A logical choice for the power-law index might be -2 which would yield an equal amount of integrated power in surface irregularities on all spatial scales (in two dimensions). The range of spatial scales over which the power-law extends would determine the band-width over which the surface should function. The peak-to-peak surface excursions should correspond to the maximum wavelength for which the surface should be effective.

We have produced a trial design for an isotropic reflective surface intended to be effective between wavelengths of about 70 cm and 1.5 cm, which we illustrate in Fig 11. The -2 power-law taper that was applied to the white noise field has been truncated at a radius of 5 pixels so as to provide about five by five of the largest scale fluctuations in the surface after Fourier transformation. The physical dimensions of the depicted surface would be about 3.5 m on a side with maximum peak-to-peak fluctuations of about 70 cm. The power-law extends down

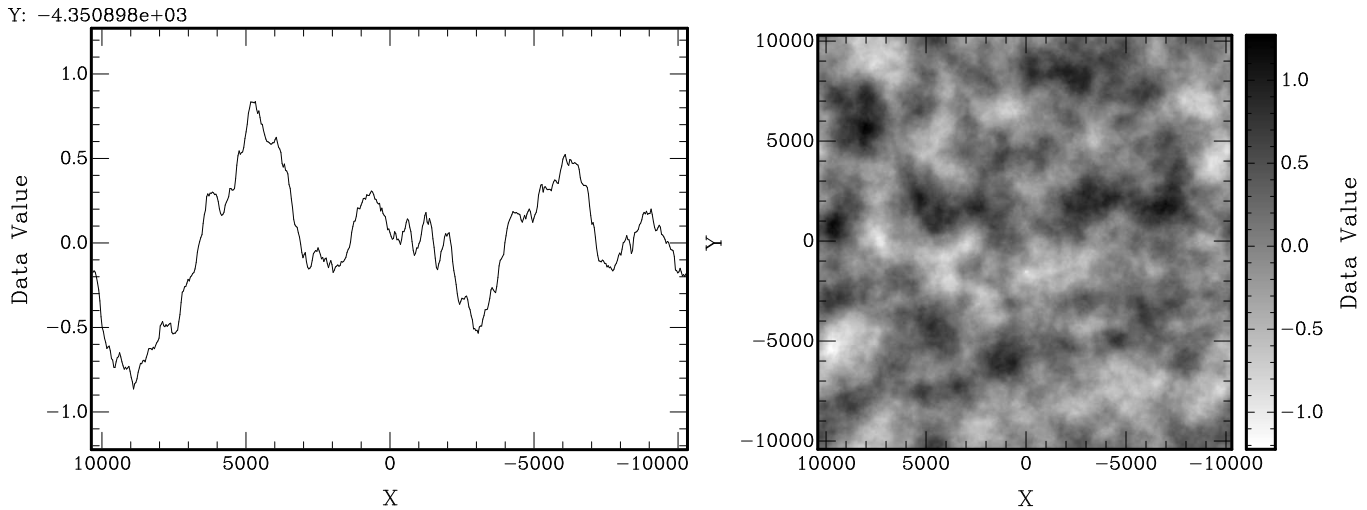


Fig. 11. Trial design for an isotropic reflective surface treatment. The image at right represents a white noise field after tapering with a -2 power-law of radius (truncated at 5 pixels from the origin) and Fourier transformation. At left is a representative cross-cut of the surface to better illustrate the range of structures present. To provide performance between observing wavelengths of 70 and 1.5 cm the surface should have spatial dimensions of about 3.5 m on a side and maximum peak-to-peak excursions of about 70 cm.

to size scales of 0.7 cm which should still provide the desired scattering properties at 1.5 cm wavelength. If regions larger than 3.5 m were being equipped with such a surface treatment they would ideally be taken from a larger input noise field, to minimize edge effects between “tiles” as well as any repetition of the tiling pattern (that might introduce grating-like responses in special directions).

We have embarked on fabrication of a scale-model of the illustrated surface design, which will be subject to measurement in a test range. If the expected broad-band scattering properties are confirmed, we will pursue full scale deployment of this surface treatment on the Parkes telescope. Perhaps the era of “standing waves” limiting performance in radio telescopes is approaching an end.

Acknowledgements. We would like to thank Hans van Someren Greve for developing software for holographic data reduction (MSHOLOG) and adjusting it for our purposes. We made extensive use of this tool. Furthermore we thank John Romein for adding support for empirical beam models into several tasks in the “Miriad” package. This permitted us to efficiently test the application of our model to real images. We are grateful to Michael Kesteven for useful comments on the original manuscript. The Westerbork Synthesis Radio Telescope is operated by the ASTRON (Netherlands Foundation for Research in Astronomy) with support from the Netherlands Foundation for Scientific Research (NWO).

References

- Braun, R., Oosterloo, T. A., Morganti, R., Klein, U., & Beck, R. 2007, *A&A*, 461, 455
- Briggs, F. H., Sorar, E., Kraan-Korteweg, R. C., & van Driel, W. 1997, *Publications of the Astronomical Society of Australia*, 14, 37
- Condon, J. J., Cotton, W. D., Greisen, E. W., et al. 1998, *AJ*, 115, 1693
- Cornwell, T. 1989, in *Synthesis Imaging in Radio Astronomy*, Vol. 6, 277–
- Hartmann, D., Kalberla, P. M. W., Burton, W. B., & Mebold, U. 1996, *A&AS*, 119, 115
- Higgs, L. A. 1967, *Bulletin of the Astronomical Institutes of the Netherlands Supplement Series*, 2, 59
- Kalberla, P. M. W., Mebold, U., & Reich, W. 1980, *A&A*, 82, 275
- Kraus, J. D. 1986, *Radio astronomy* (Powell, Ohio: Cygnus-Quasar Books, 1986)
- Napier, P. J. 1999, in *ASP Conf. Ser. 180: Synthesis Imaging in Radio Astronomy II*, 37–
- Raimond, E. 1966, *Bulletin of the Astronomical Institutes of the Netherlands Supplement Series*, 1, 33
- Sault, R. J., Teuben, P. J., & Wright, M. C. H. 1995, in *ASP Conf. Ser. 77: Astronomical Data Analysis Software and Systems IV*, 433–
- Scott, P. F. & Ryle, M. 1977, *MNRAS*, 178, 539
- Thompson, A. R., Moran, J. M., & Swenson, G. W. 1986, *Interferometry and synthesis in radio astronomy* (New York, Wiley-Interscience, 1986, 554 p.)
- van Woerden, H. 1962, *De neutrale waterstof in Orion* (Groningen: Rijksuniversiteit, 1962)
- van Woerden, H., Takakubo, K., & Braes, L. L. E. 1962, *Bull. Astron. Inst. Netherlands*, 16, 321